



Highly efficient p-type Cu₃P/n-type g-C₃N₄ photocatalyst through Z-scheme charge transfer route

Shixin Hua, Dan Qu, Li An*, Wenshuai Jiang, Yuanjing Wen, Xiayan Wang, Zaicheng Sun*

Beijing Key Laboratory of Green Catalysis and Separation, Department of Chemistry and Chemical Engineering, College of Environmental and Energy Engineering, Beijing University of Technology, Beijing, 100124, China



ARTICLE INFO

Keywords:

Cu₃P
g-C₃N₄
Cocatalyst
Z-scheme
Charge transfer

ABSTRACT

Phosphides exhibit relatively low overpotential for electrical hydrogen evolution reaction (HER), thus they have great potential to be used for cocatalyst for photocatalyst. Cu₃P, as a p-type semiconductor, tends to form a p-n junction with an n-type photocatalyst. Typically, it is treated as a sensitizer to extend the light absorption. However, its function and work mechanism are not fully understood in the catalyst system. In this report, we synthesized g-C₃N₄ and loaded Cu₃P nanoparticle on its surface. The photoluminescence (PL) spectra, photocurrent and electrochemical impedance spectra confirm the Cu₃P greatly enhance the charge separation process. Electrochemical HER results indicate that the composites have lower over-potential for HER. These results confirm the Cu₃P works as a cocatalyst in the system, not a sensitizer. Further, we tracked the photogenerated electron transfer direction via photodeposition of Pt nanoparticles. The Pt nanoparticles tend to deposit near the Cu₃P nanoparticles. That illustrates the photogenerated electron will be left on Cu₃P nanoparticles. On the other hand, the photocatalytic decomposition of Rhodamine B (RhB) illustrates that the holes are left on the g-C₃N₄ due to both g-C₃N₄ and Cu₃P/g-C₃N₄ have similar decomposition rate, but the Cu₃P cannot decompose RhB. Based on these, we proposed the photogenerated electron of g-C₃N₄ recombine with the hole of Cu₃P, the photogenerated electron of Cu₃P will be left for HER. That reasonably explain the cocatalyst function of Cu₃P in the composite catalyst system.

1. Introduction

Facing the shortage of energy, utilizing infinite solar energy is a possible and promising solution. Photocatalytic water splitting is an environmental friend technique to convert solar energy into hydrogen energy which maintains a clean energy cycle. Thus, photocatalytic H₂ production has become a promising research area since it was reported by Fujishima and Honda in 1972 [1]. Among various semiconductor-based photocatalysts like metal oxides [2,3] (TiO₂ [4], SrTiO₃ [5,6], BiVO₄, [7] BiClO [8,9] etc.), metal sulfides [10] (CdS, ZnCdS, CuInS₂ etc.) and oxynitrides and oxysulfides [11,12], graphite carbon nitride (g-C₃N₄) as a metal-free catalyst exhibit relatively wide light absorption band super stability for H₂ production. However, poor charge separation efficiency and high over-potential for the reduction and oxidation reaction result in a low activity of the catalyst. The cocatalyst is usually loaded onto the surface of semiconductors to accept the photogenerated electron and enhance charge separation. At the same time, hydrogen reduction reaction (HER) happens on the cocatalysts, which lower the over-potential of HER. Based on these two functions, various noble

metals such as Pt, Rh, Pd, Ru, Ag and Au have been employed as an efficient electron sink to promote charge separation because noble metals with large work function, for example, Pt, are ready to accept and trap electrons [13–16]. A Schottky barrier can be formed at the metal/photocatalyst interface. The Schottky barrier is a kind of junction which can promote charge separation of photogenerated electron and hole. The photogenerated electron can be easily transferred from photocatalyst to the noble metal. On the other hand, they possess a relatively low overpotential for hydrogen evolution reaction (HER). Thus, noble metals e.g. Pt, are treated as the most suitable cocatalyst for photocatalytic H₂ production.

However, the high prices of noble metals seriously barrier their practical application. It is highly demanded to look for the replacement. During the past decades, electrochemical water splitting is rapidly developed in the seeking low over-potential electrode materials. A number of materials based on the transition metals (e.g. Fe, Co, Ni, Cu, Mo) have been demonstrated as a promising electrode material for HER due to relatively low over-potential [17]. Some of them have been developed as a robust cocatalyst such as MoS₂ [18], Ni-based materials

* Corresponding author.

E-mail addresses: 08131@bjut.edu.cn (L. An), sunzc@bjut.edu.cn (Z. Sun).

[19–21] and cobalt-based materials [22–24]. Very recently, transition metal phosphides have emerged as low-cost catalysts for water splitting (both HER and OER). In 2013, Chen and coworkers [25,26] first demonstrate the mixture of Ni₂P colloidal nanoparticles and CdS nanorods for constructing photocatalytic system through collision-contact mechanism to promote charge separation [27]. And then, Ni₂P [28,29], CoP [30,31], Fe₂P [32], FeP [33] and NiCoP [34,35] are employed as the cocatalyst for enhanced photocatalytic H₂ evolution. As an n-type semiconductor, these phosphides is favorable to accepting the photo-generated electron. Meanwhile, they also have relatively low over-potential for HER. Thus, the enhanced photocatalytic activity is demonstrated. Cu₃P [32,36] is also loaded on the surface photocatalyst (TiO₂ and CdS) and catalyst composites exhibit enhanced photocatalytic activities. Typically, Cu₃P is treated as p-n junction instead of cocatalyst since Cu₃P is a p-type semiconductor. If so, the photogenerated electron tends to transfer from Cu₃P to TiO₂. However, TiO₂ exhibit quite low photocatalytic performance in the absence of the cocatalyst. It is worth to investigate the function of Cu₃P and understand the enhancement mechanism of photocatalytic performance.

In this report, we chose the high surface area graphite carbon nitride (g-C₃N₄) as an n-type photocatalyst, successfully loaded the Cu₃P nanoparticles through chemical deposition-phosphorization processes. Photoluminescence spectra (PL), photocurrent and electrochemical impedance spectroscopy (EIS) Nyquist plots clearly proved that the charge separation process is greatly enhanced after loading Cu₃P. Electrocatalytic HER was carried out to illustrate that Cu₃P effectively lower the over-potential of g-C₃N₄ for HER reaction, indicating Cu₃P is a potential cocatalyst. If Cu₃P is a cocatalyst, the photogenerated electron will transfer from g-C₃N₄ (n-type) to Cu₃P (p-type). To verify this, the electron flow direction was tracked by photodeposition of Pt nanoparticles. The results disclose that the Pt nanoparticles are photo-deposited besides the Cu₃P nanoparticles, indicating the photo-generated electron will keep at the site of Cu₃P. To understand this phenomenon, we proposed the photogenerated charge transfer follows the direct Z-scheme route. That is, the photogenerated electrons from g-C₃N₄ recombine with the holes of Cu₃P and the photogenerated electrons from Cu₃P will be left for HER. It provides new insights into design and understanding the nanostructure photocatalyst.

2. Experimental section

2.1. Synthesis of the photocatalyst

2.1.1. Preparation of graphitic carbon nitride (g-C₃N₄)

Typically, 20 g of thiourea and 20 g ammonium chloride were ground uniformly and put into a mortar. The mixtures were transferred to an alumina crucible with a cover and heated to 550 °C for 4 h in a muffle furnace at a temperature rate of 1 °C/min. After the reaction was completed, a yellow solid powder was obtained, that was g-C₃N₄. The thermal treatment of g-C₃N₄ in a corundum porcelain boat. The g-C₃N₄ was put in a muffle furnace and heated to 500 °C for 4 h with a ramp rate of 2 °C/min to complete the reaction. After the reaction was completed, a light yellow solid powder was obtained, which was denoted as g-C₃N₄ nanosheets. The synthesis route of g-C₃N₄ nanosheets shown in Scheme 1.

2.1.2. Preparation of Cu₃P/g-C₃N₄ composite materials

First, the g-C₃N₄ nanosheets sample (200 mg) was dispersed in 50 mL of deionized water and sonicated for 2 h. Then, designed amount of copper chloride in aqueous solution was added in the above solution slowly with a copper loading of 0.5, 1.0, 2.0, or 3.0 wt%. After magnetic stirring for 2 h at room temperature, a certain amount of NH₃·H₂O (0.1 M) aqueous solution was added dropwise according to the copper loading with a molar ratio of NH₃·H₂O:Cu²⁺ at 2:1 and followed by magnetic stirring for 1 h, the suspension was filtered, washed with deionized water for several times. The obtained solid precursor was

further dried in a vacuum freeze-dried for 24 h. Subsequently, the Cu₃P/g-C₃N₄ composites were synthesized using the above solid precursor as the reactant for phosphorization. In detail, 200 mg of the prepared precursor and 200 mg of NaH₂PO₂·H₂O were blended mechanically and ground into fine powder. Then, the fine powder was annealed at 300 °C for 3 h in a quartz tube with a heating rate of 2 °C/min under Ar flow. The obtained products were washed with deionized water to remove residual salts, and dried in a vacuum freeze-dried for 24 h.

The pure Cu₃P was also prepared using a similar procedure.

2.1.3. Preparation of 1.0 wt% Pt/g-C₃N₄ composites

First, the g-C₃N₄ nanosheets sample (200 mg) was dispersed in 50 mL of deionized water and sonicated for 2 h. Then, 1.0 wt% Pt was using H₂PtCl₆ dissolved in the solution. After magnetic stirring for 2 h at room temperature, newly prepared of NaBH₄ (0.1 M) aqueous solution was added dropwise according to the platinum loading with a molar ratio of NaBH₄:Pt⁴⁺ at 5:1 and followed by magnetic stirring for 1 h, the suspension was filtered, washed with deionized water for several times. The resultant solid precursor was further dried in a vacuum freeze-dried for 24 h.

2.1.4. Charge flow tracking by photodeposition

Photo-deposition of 0.5 wt% Pt on the surfaces of CC-1.0 were carried out using H₂PtCl₆ as a precursor. Typically, 10 mg of CC-1.0 and a calculated amount of metal precursor were dispersed in 100 mL of 10 vol% methanol aqueous solution under stirring. The suspension was then irradiated by a 300 W Xe lamp with reaction temperature maintained at 5 °C by cycle cooling water equipment. After 2 h photo-deposition, the suspension was filtered, washed with deionized water several times, and finally dried in the oven at 60 °C overnight.

2.2. Photocatalytic activity characterization

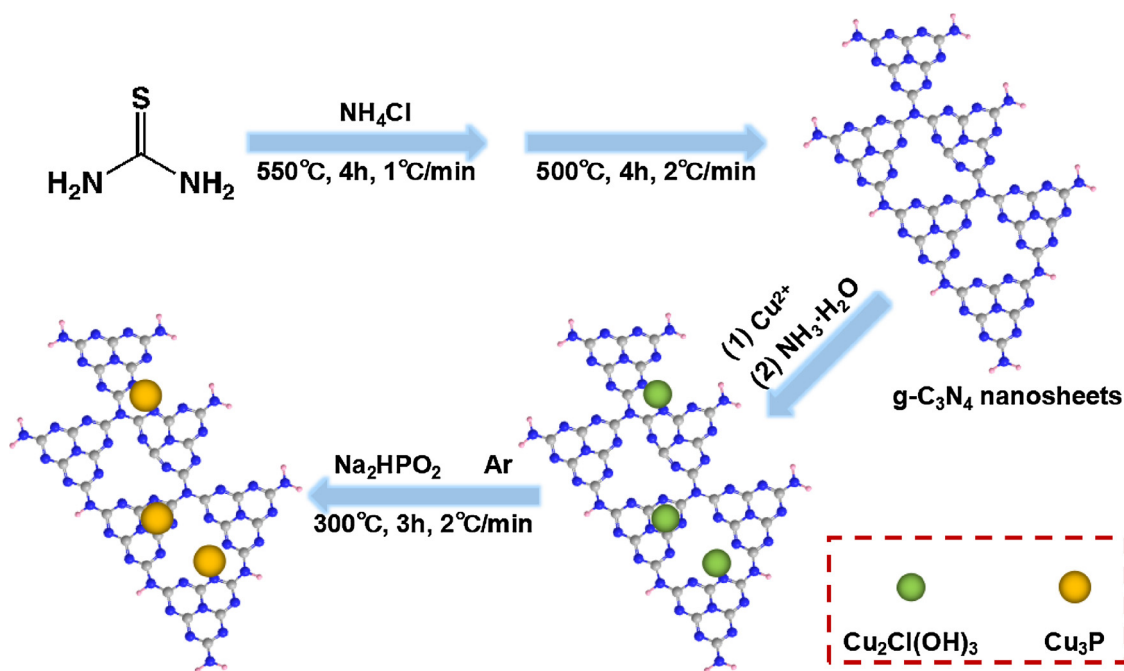
Photocatalytic hydrogen evolution via water-splitting was performed in a closed Pyrex glass reactor. For investigations of photocatalytic performance, the well-ground photocatalyst (10 mg) was suspended in an aqueous solution of TEOA (10 vol%, 100 mL) under vigorous stirring. A 300 W Xe lamp was also utilized as the visible light source for irradiation with a 420 nm cut-off filter for the photocatalytic reactions. The temperature of the reactant solution was maintained at 5 °C by a flow of cycle cooling water system during the reaction. The amount of hydrogen produced was determined by gas chromatography (Shimadzu GC-2014C), using a thermal conductivity detector (TCD) with N₂ as the carrier gas.

The stability test of the as-prepared composite materials (10 mg) of CC-1.0 was operated in the H₂ production system using TEOA (10 vol%, 100 mL) aqueous solution as electron donor.

Wavelength-dependent H₂ evolution measurement was also operated in the H₂ production system with a band-pass filter for 380 nm, 420 nm, 475 nm, 500 nm, respectively. The as-prepared composite materials (10 mg) of CC-1.0 and 1.0 wt% Pt/g-C₃N₄ were operated in the H₂ production system in TEOA (10 vol%, 100 mL) aqueous solution.

2.3. Photoelectrochemical measurements

The photoelectrochemical measurements were conducted with an Autolab PGSTAT302 N in a conventional three-electrode system under visible light assembled by a 300 W Xe lamp with a 420 nm cutoff filter. Ag/AgCl electrode, carbon electrode, and phosphate buffered solution (PBS) (pH = 7.00) were used as the reference electrode, counter electrode, and electrolyte, respectively. To prepare the working electrode, the photocatalyst (4 mg) and 5 wt% Nafion solution (80 μL) were dispersed in isopropyl alcohol (920 μL) and sonicated for at least 1 h to form a homogeneous mixture [37]. Then, the mixture (40 μL) was drop-casted on a 4 cm × 1 cm FTO (fluorine-doped tin oxide) glass electrode



Scheme 1. Synthesis route of Cu₃P/g-C₃N₄ composites photocatalyst.

and left to dry at room temperature. FTO glass substrates with the coated area about 1 × 1 cm² are used for electrodes.

Cyclic voltammograms (CVs) were recorded between -0.6 and -1.2 V versus Ag/AgCl (saturated KCl) at a scan rate of 100 mV/s. CVs were scanned for 50 cycles. Linear sweep voltammograms (LSVs) were measured from -0.6 to -1.4 V versus Ag/AgCl (saturated KCl) with a scan rate of 5 mV/s. Electrochemical impedance spectroscopy (EIS) tests were conducted in the same configuration at η = -0.6 V (vs. RHE) from 10⁵–10⁻¹ Hz with an AC voltage of 20 mV. Transient photo-currents measurement were conducted in the same configuration at η = 0.5 V versus Ag/AgCl (saturated KCl). Mott-Schottky were recorded between -1.6 and 0.0 V versus Ag/AgCl (saturated KCl). All the potentials were calibrated with the RHE using the equation E_{vs. RHE} = E_{vs. Ag/AgCl} + E_{Ag/AgCl} + 0.059 pH.

2.4. Characterizations

The crystal structure of the samples was investigated using X-ray diffraction (XRD; Bruker D8 Advance X-ray diffractometer) with Cu Kα radiation ($\lambda = 0.15406$ nm) as the incident beam at 40 kV and 40 mA. The morphology of the samples was examined by transmission electron microscopy (TEM; FEI Tecnai G2 F20) operated at 200 kV and Tecnai G2 F30 S-Twin microscope attached with an OXFORD MAX-80 energy dispersive X-ray (EDX) system. Scanning electron microscope (SEM; Hitachi SU-8010) operated at 5 kV. UV-vis diffuse reflection spectroscopy (DRS) was performed on a Shimadzu UV-2600 spectrophotometer using BaSO₄ as the reference. The photoluminescence (PL) spectra of the photocatalyst were obtained by a Hitachi F-7000 with an excitation wavelength of 325 nm. BET specific surface area is measured using a Quantachrome Surface Area and Pore Size Analyzer (Quantachrome Instrument version 3.01). XPS measurements were conducted on a Kratos Axis-Ultra multifunctional X-ray spectrometer. All binding energies were referenced to the C 1 s peak at 284.8 eV.

3. Results and discussion

Scheme 1 shows synthetic routes of high surface area Cu₃P/g-C₃N₄. Two-step pyrolysis reaction was taken to prepare g-C₃N₄ nanosheets with high surface area due to the gases released were released by

decomposing NH₄Cl at high temperature. Furthermore, the porous g-C₃N₄ were thermally treated at 500 °C for 4 h to form thin g-C₃N₄ nanosheets. When g-C₃N₄ nanosheets were placed into the CuCl₂ solution, the amino group on the g-C₃N₄ can form complexes with Cu²⁺. This complexes converted into Cu₂Cl(OH)₃ nanoparticles when the solution was adjusted to the base by adding the NH₃·H₂O aqueous solution. Furthermore, the Cu₂Cl(OH)₃ was converted into Cu₃P by thermal treating the mixture of Cu₂Cl(OH)₃/g-C₃N₄ and NaH₂PO₂ at 300 °C for 2 h. The obtained Cu₃P/g-C₃N₄ samples were denoted as CC-0.5, 1.0, 2.0, 3.0 with different amount of Cu₃P in the composites, respectively.

Generally, the dense g-C₃N₄ with the low surface area was obtained by pyrolysis of thiourea in the inert environment. The large surface area will generate more active sites and efficient charge separation efficiency. To achieve large surface area, pore forming materials - NH₄Cl was introduced into the reaction. Furthermore, the additional thermal treatment was applied to prepared g-C₃N₄ nanosheets at 500 °C in the air. As shown in Fig. S1, scanning electron microscopy (SEM) and transmission electron microscopy (TEM) images clearly show as-prepared g-C₃N₄ exhibits nanosheets morphology, which is kept after loading the 1.0 wt% Cu₃P. Fig. 1a illustrates the X-ray diffraction (XRD) pattern of g-C₃N₄ and Cu₃P/g-C₃N₄ (CC-0.5 ~ 3.0). The characteristic diffraction peaks of g-CN at 13.1° and 27.6° are observed. It is hardly found the diffraction peak in the composites samples due to low loading amount. Pure Cu₃P was prepared in the same synthesis route, which shows feature diffraction peaks of hexagonal Cu₃P (Fig. S2). Fig. 1b shows the N₂ sorption isotherm curves of g-C₃N₄ and CC-1.0 sample. Both of them exhibit type IV isotherms with H3 type hysteresis loop, which is associated with capillary condensation in the mesoporous structure. They do not exhibit any limiting adsorption at high relative pressure, which is observed with aggregates of plate-like particles giving rise to slit-shaped pores [38]. Brunauer-Emmett-Teller (BET) surface area of g-C₃N₄ and CC-1.0 are 91.3 and 87.9 m² g⁻¹, respectively. The corresponding pore size distribution plot is shown as inset of Fig. 1b. The size of mesopore is ~ 2.7 nm for both g-C₃N₄ and CC-1.0. These indicate that the loading process of Cu₃P did not change the morphology of g-C₃N₄.

Fig. 1c-e display transmission electron microscopy (TEM) and high resolution (HR) TEM images of CC-1.0. Cu₃P nanoparticles with the average size of 15.5 ± 7.1 nm are uniformly dispersed on the g-C₃N₄

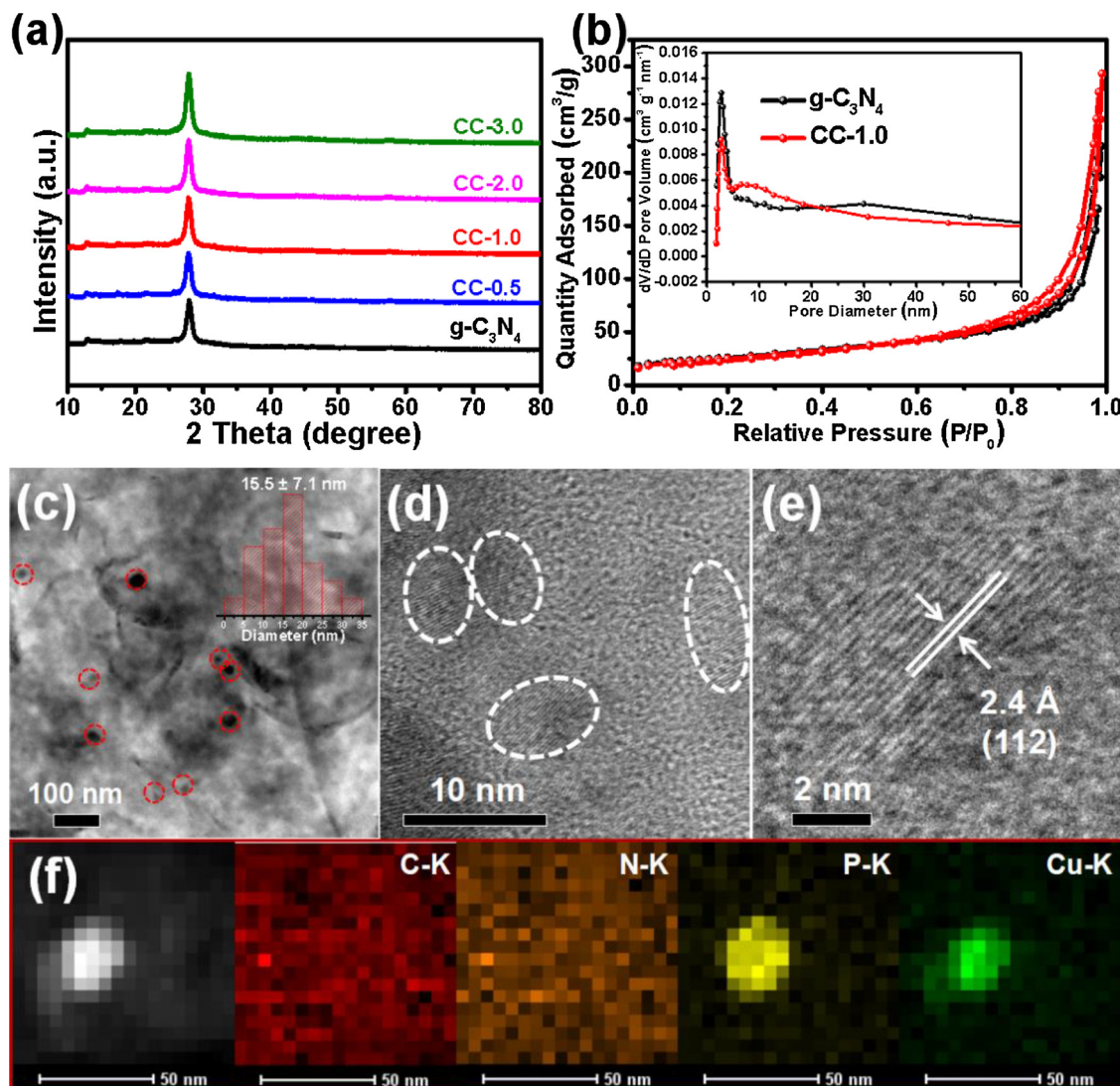


Fig. 1. (a) XRD patterns of pure g-C₃N₄ and different loading amount of Cu₃P on g-C₃N₄ samples (CC-0.5–3.0: 0.5–3.0 wt% Cu₃P/g-C₃N₄); (b) Nitrogen adsorption-desorption isotherms of the g-C₃N₄ and CC-1.0 samples and the corresponding pore size distribution plot (the inset). Transmission electron microscopy (TEM, c) and high-resolution TEM (d, e) image of Cu₃P/g-C₃N₄ (CC-1.0). (f) TEM image of Cu₃P/g-C₃N₄ and corresponding C, N, P, Cu element mapping.

nanosheets. HR TEM images illustrate the lattice fringe spacing of 0.24 nm corresponding to the (112) lattice fringe of Cu₃P. To further confirm the element composition, EDX elemental mapping images (Fig. 1f) clearly show the distribution of C, N, P and Cu. The C and N elements spread all over the images indicating the matrix is composed of C and N. The P and Cu mainly concentrate at the site of the bright spot in the corresponding TEM image, indicating that the particle is composed of Cu and P.

To further verify the chemical composition and electronic state of the Cu₃P/g-C₃N₄ samples, X-ray photoelectron spectroscopy (XPS) was conducted. As shown in Fig. S3, the full survey XPS spectrum discloses that CC-1.0 is composed of C (284 eV), N (399 eV), Cu (932) and P (133 eV). High-resolution C1s, N1s, Cu2p and P2p XPS of CC-1.0 are displayed as Fig. 2. High-resolution C1s XPS spectrum (Fig. 2a) can be fitted as 4 dominant peaks at 284.6, 286.1, 287.8 and 288.6 eV, corresponding to sp² C in g-C₃N₄ (C–C), sp³ C (C–NH₂), N=C=N and –COOH [39,40]. The peaks at 398.2, 399.3, 400.8, 403.9 eV in N1s XPS spectrum are assigned to sp² hybridized nitrogen (C=N=C), bridging N atoms in tertiary nitrogen N-(C)₃, terminal amino functions (–C-N-H) and positive charge localization or the charging effects in the cyano-group and heterocycles [34,41]. Two peaks at 932.1 and 951.8 eV are contributed from Cu 2p_{3/2} and 2p_{1/2}, respectively, which

are matched with the Cu₃P signal. However, only one weak peak was observed at 132.5 eV in the P2p XPS spectrum of CC-1.0 due to low loading amount on the g-C₃N₄. Similar results were observed in the previous reports [36,42]. It was attributed this peak to the P2p species with partial oxidation because it is hard to distinguish the P2p_{3/2} and P2p_{1/2} in the case of less amount of Cu₃P. Based on the above results, Cu₃P nanoparticles are successfully loaded on the surface of g-C₃N₄.

As shown in Fig. 3a and b, the loading of Cu₃P on g-C₃N₄ significantly enhances the photocatalytic H₂ production performance ($\lambda > 420$ nm). With pure g-C₃N₄, only 10.8 $\mu\text{mol g}^{-1} \text{h}^{-1}$ can be produced, indicating that most photogenerated charges take recombination route. The H₂ evolution rate can be greatly enhanced to over 60 folds by loading 0.5 wt% Cu₃P nanoparticles to the g-C₃N₄ nanosheets. It reaches maximum 808 $\mu\text{mol g}^{-1} \text{h}^{-1}$ with 1.0 wt% of Cu₃P loading and then decreases gradually. It probably due to the shielding effect of light absorption by excess Cu₃P on the surface of g-C₃N₄ [43]. For comparison, 1.0 wt% Pt was loaded on g-C₃N₄ via similar chemical (denoted as Pt/g-C₃N₄). The H₂ evolution rate only reaches 658 $\mu\text{mol g}^{-1} \text{h}^{-1}$ for Pt/g-C₃N₄. That indicates the Cu₃P could be a potential replacement for noble Pt. Furthermore, the photocatalytic activity of Cu₃P/g-C₃N₄ exhibits no obvious decrease after four consecutive cycles, indicating Cu₃P/g-C₃N₄ has superior stability. Since Cu₃P is a narrow bandgap

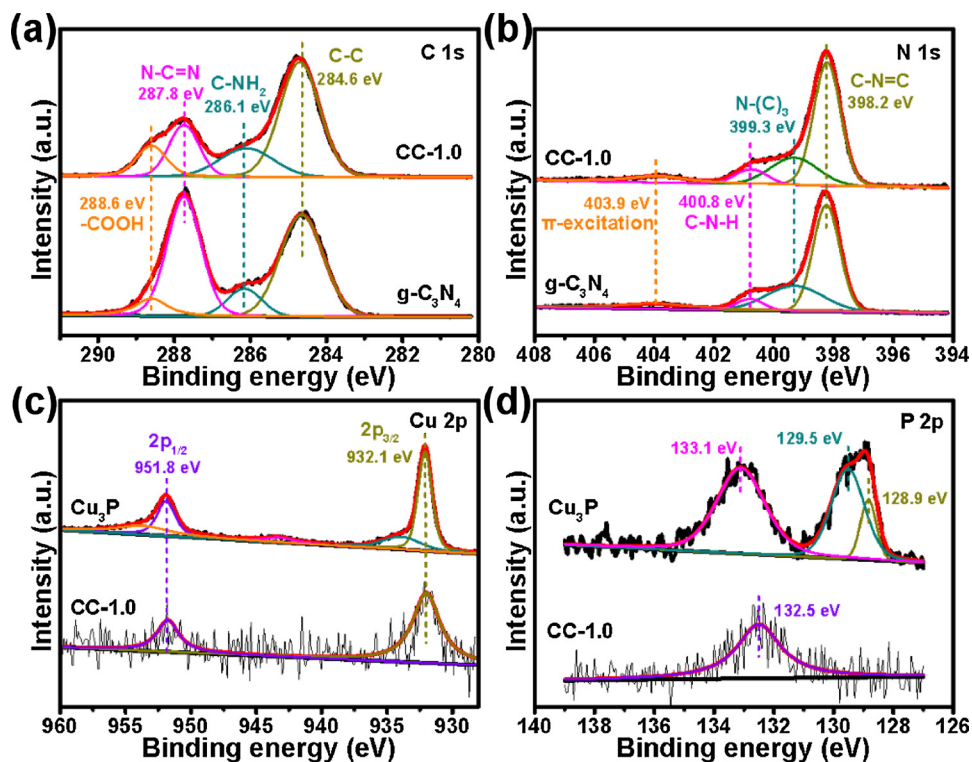


Fig. 2. High resolution C1 s (a), N1 s(b), Cu2p (c) and P2p (d) X-ray photoelectron spectroscopy (XPS) spectra of g-C₃N₄, Cu₃P and Cu₃P/g-C₃N₄ (CC-1.0).

semiconductor, it may contribute to the light absorption on the catalyst. To verify that, the dependence of H₂ production on the wavelength was investigated for the CC-1.0 and Pt/g-C₃N₄. As shown in Fig. 3d, both CC-1.0 and Pt/g-C₃N₄ have similar photo response range from UV to 550 nm. However, CC-1.0 exhibits more H₂ production capability at each wavelength. These results indicate that The main contribution of Cu₃P is the enhancement of the charge separation process, not the extension of light absorption.

To further confirm that, photoluminescence (PL) spectra of g-C₃N₄

and Cu₃P/g-C₃N₄ are shown in Fig. 4a. The PL intensity of g-C₃N₄ dramatically decreases after loading Cu₃P nanoparticles, indicating that the radiation recombination is greatly depressed due to enhanced charge separation. Fig. 4b illustrates the photocurrent density-time (i-t) curves of the Cu₃P/g-C₃N₄ and the g-C₃N₄ working electrode, which are measured 0.5 V vs. Ag/AgCl under visible light irradiation ($\lambda > 420$ nm). It clearly displays that the photocurrent density produced from Cu₃P/g-C₃N₄ is much higher than that of g-C₃N₄, implying a distinct improvement in the suppression of photo-generated electron-

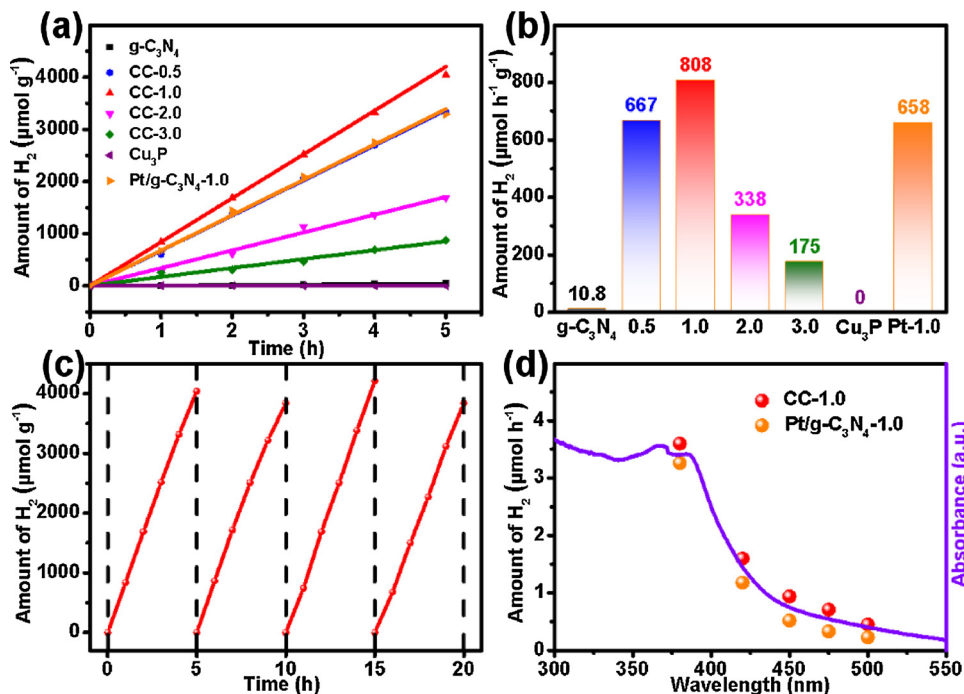


Fig. 3. (a) Normalized H₂ evolution amount-time plots and normalized H₂ evolution rate (b) of g-C₃N₄, Cu₃P and Cu₃P/g-C₃N₄ (CC-0.5 ~ 3.0). Pt/g-C₃N₄-1.0 and Pt-1.0 are the g-C₃N₄ nanosheets loaded 1.0 wt% Pt nanoparticles. The stability test of CC-1.0 (c), the H₂ production was recorded in the continuous four cycles. (d) the dependence of the H₂ production rate on the wavelength of CC-1.0 (red dots) and chemical deposition of Pt/g-C₃N₄-1.0 (orange dots), the purple line is the UV-vis spectrum of CC-1.0, corresponding to the right axis.

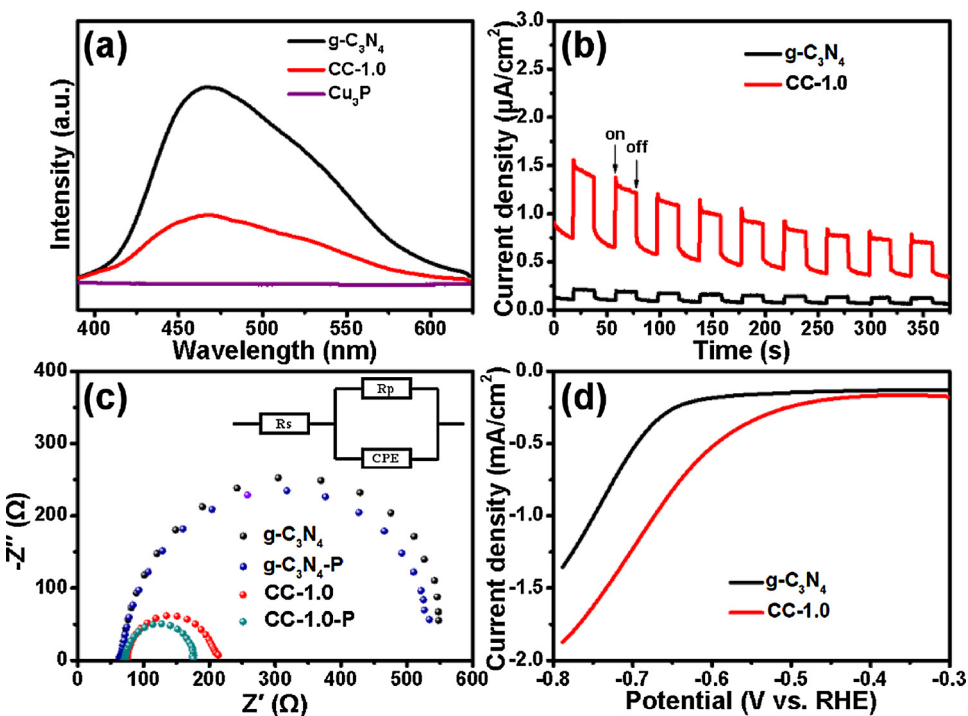


Fig. 4. (a) Photoluminescence spectra of g-C₃N₄, Cu₃P and CC-1.0; (b) current density-time plots of g-C₃N₄ and CC-1.0; (c) Electrochemical impedance spectroscopy (EIS) of g-C₃N₄ and CC-1.0. -P stands for the measurements were carried out under light illumination; (d) electrochemical HER reaction of g-C₃N₄ and CC-1.0.

hole recombination. That well consists of the PL results. Furthermore, electrochemical impedance spectroscopy (EIS) Nyquist plots of g-C₃N₄ and Cu₃P/g-C₃N₄ are displayed in the Fig. 4c. Both g-C₃N₄ and Cu₃P/g-C₃N₄ exhibit semicircles in the middle-frequency region. The arc radius on the Nyquist plot of Cu₃P/g-C₃N₄ is smaller than that of g-C₃N₄, indicating that a slower charge recombination and a more efficient charge separation for the Cu₃P/g-C₃N₄. It should be noted that the arc radius further decreases under photoirradiation. Based on these results, it implies that Cu₃P loading greatly promotes the charge separation process in the catalyst. Another important feature of cocatalyst is lowering the overpotential of HER on the surface of the photocatalyst. According to Sun's report [44,45], nanostructural Cu₃P has lower overpotential for electrocatalytic HER. To gain insight into the water electrolysis activity of Cu₃P/g-C₃N₄ and g-C₃N₄, the electrocatalytic HER were evaluated by using a three-electrode system. Fig. 4d shows the Cu₃P/g-C₃N₄ exhibits higher activity than g-C₃N₄. The starting potentials for HER are -0.65 V vs. RHE and -0.45 V vs. RHE for g-C₃N₄ and Cu₃P/g-C₃N₄, respectively. The current density of -1.0 mA cm⁻² can be achieved at overpotential as low as -0.67 V vs. RHE on Cu₃P/g-C₃N₄, which is smaller than that on pure g-C₃N₄ (-0.75 V vs. RHE). Lower over-potential of Cu₃P/g-C₃N₄ demonstrate that the hydrogen reduction reaction more easily happens on the Cu₃P/g-CN than that on g-C₃N₄. On the basis of above results, Cu₃P nanoparticles have two functions in this catalyst: one is promoting charge separation, another is lower the overpotential of HER. Thus, it mainly works as a cocatalyst on the photocatalytic hydrogen evolution of Cu₃P/g-C₃N₄. However, Cu₃P is usually a p-type semiconductor and g-C₃N₄ is an n-type semiconductor. A p-n junction will form by putting these two together, and then the photogenerated electron easily flows from p-type semiconductor to the n-type one. If Cu₃P work as a cocatalyst, the photogenerated electron should flow from g-C₃N₄ to Cu₃P, and the HER reaction carries out on the Cu₃P site. These two case are contradictory.

To disclose the charge flow direction, the energy level of the Cu₃P and g-C₃N₄ need to be first known. The optical properties are investigated to make determine the energy level of Cu₃P and g-C₃N₄. Fig. 5a and b show diffuse reflectance spectroscopy (DRS) UV-vis

spectra of g-C₃N₄, Cu₃P/g-C₃N₄ and Cu₃P. The corresponding Tauc plots are displayed as insets. Cu₃P exhibits broad absorption in the whole visible light region due to the presence of vacancies. Comparing with g-C₃N₄, Cu₃P/g-C₃N₄ shows similar spectrum as g-C₃N₄ besides the slight increase of the baseline. These results illustrate Cu₃P has a slight contribution to the light absorption in the composites. It is noted that the absorption edge of g-C₃N₄ is almost unchanged after decoration of Cu₃P nanoparticles on the surface, indicating that it does not form Cu and P atoms doped g-C₃N₄. The band gap of composite has no change with g-C₃N₄. The optical band gap can be drawn from the Tauc plot. They are 2.79 and 1.41 eV for g-C₃N₄ and Cu₃P, respectively. valence band (VB) XPS spectra are exhibited in the Fig. 5c and d. The VB position of g-C₃N₄ and Cu₃P are 1.71 and 0.89 eV, respectively. Due to the cation vacancies, the tail response is observed in the VB XPS spectrum of Cu₃P. The conduction band (CB) positions of g-C₃N₄ and Cu₃P were calculated to be -1.0 and -0.51 eV, respectively, according to the equation: $E_{VB} = E_{CB} + E_g$ [46]. The Mott-Schottky analysis is applied to identify the types of conductivity for g-CN and Cu₃P (Fig. 5e and f). Linear region of $1/C^2$ (C is the capacitance) v.s. the applied potential can be fitted with the Mott-Schottky equation. The positive slope of the line suggests n-type conductivity of g-C₃N₄, while the negative linearity implies the p-type conductivity of Cu₃P. The corresponding intercept to the x-axis provides the flatband potential, which can be taken as a reference for Fermi level of the semiconductor. As shown in Fig. 6e and f, the pure g-C₃N₄ and Cu₃P are n- and p-type semiconductors with the flatband potential of -0.86 and 0.54 V v.s. RHE.

On the basis of above results, the energy band structures of Cu₃P and g-C₃N₄ before forming junction are shown in the Fig. S5a. The Fermi level of g-C₃N₄ is higher than that of Cu₃P. When Cu₃P was loaded onto g-C₃N₄, two semiconductors has same Fermi level since heterojunction forms. Fig. S6a shows the VB XPS of CC-1.0. It discloses that the VB of CC-1.0 is about 1.71 eV indicating the VB of g-C₃N₄ was kept after loading Cu₃P onto g-C₃N₄. The Mott-Schottky plot of CC-1.0 as shown in Fig. S6b illustrates that the flatband potential turns to -0.49 eV indicating the Fermi level shift to -0.49 eV after form the junction. Then the energy level diagram of CC-1.0 will be shown in Fig.

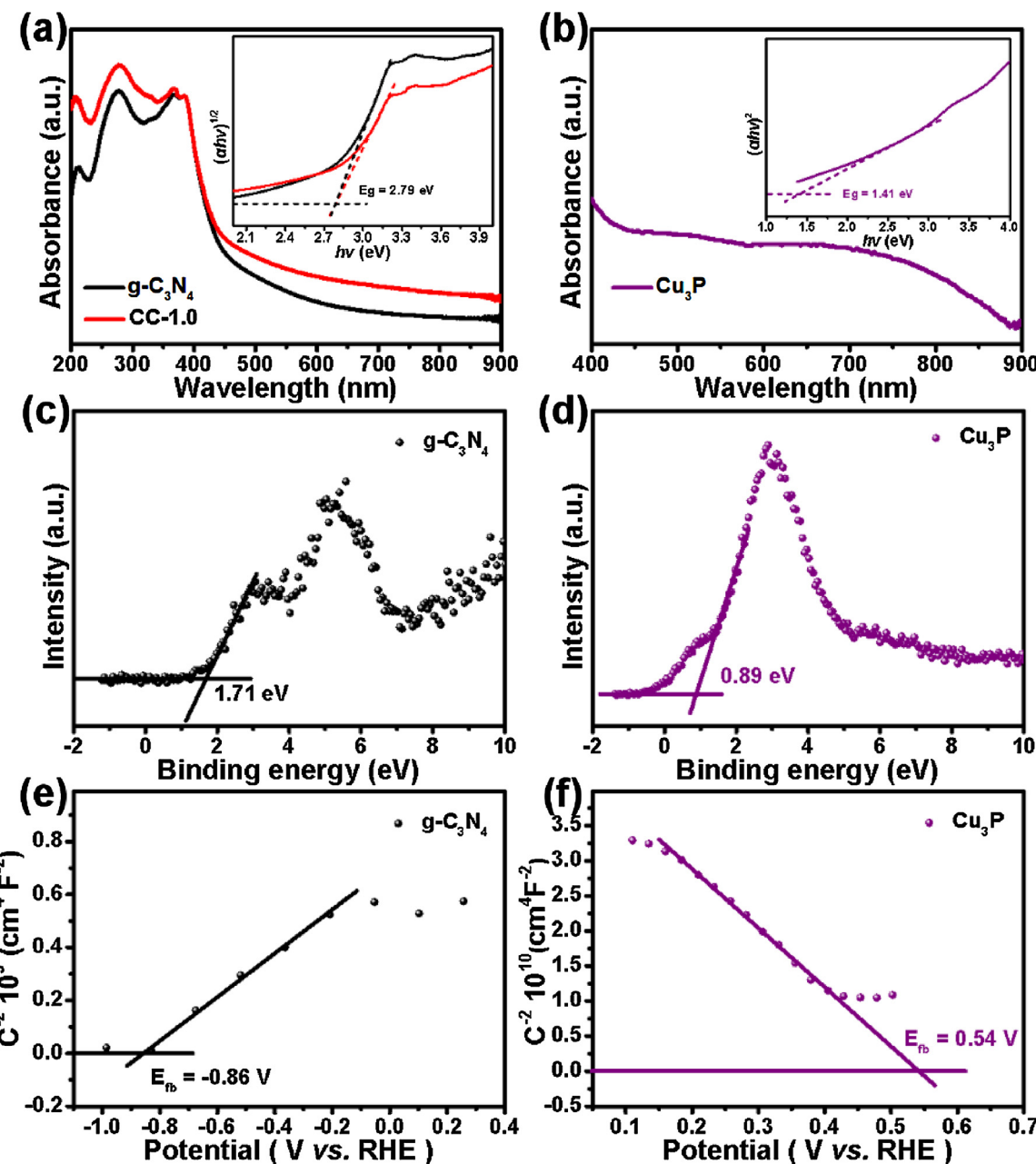


Fig. 5. (a, b) UV-vis spectra of $\text{g-C}_3\text{N}_4$, CC-1.0, and pure Cu_3P . The insets are the corresponding Tauc plots. (c, d) valance band XPS spectra of $\text{g-C}_3\text{N}_4$ and Cu_3P . (e, f) Mott-Schottky plots of $\text{g-C}_3\text{N}_4$ and Cu_3P .

S5b. In general, p-type Cu_3P contacts with n-type $\text{g-C}_3\text{N}_4$, the p-n junction is a favor to form without light irradiation [36,42,47]. If so, the photogenerated electron tends to transfer from Cu_3P to $\text{g-C}_3\text{N}_4$. Then the active site of H_2 production should locate on the $\text{g-C}_3\text{N}_4$. It seems to contradict the function of Cu_3P as a cocatalyst.

To verify the photogenerated electron transfer direction, photo-deposition of Pt nanoparticles was conducted on the $\text{Cu}_3\text{P}/\text{g-CN}$ composite catalyst. Fig. S7a and S7b show the UV-vis spectra of Rhodamine B (RhB) aqueous solution during the photocatalytic degradation with the presence of $\text{g-C}_3\text{N}_4$ and CC-1.0. CC-01.0 exhibits similar photocatalytic degradation behavior and activity for RhB as $\text{g-C}_3\text{N}_4$ (Fig. S7b). However, the Cu_3P has relatively poor photocatalytic degradation activity. In order to identify the active species in the photocatalytic degradation process, different radical scavenger and inhibitor were employed [48–50]. Among them, TEOA and IPA are the hole (h^+) and hydroxyl radical ($\cdot\text{OH}$) scavengers and N_2 is an inhibitor of superoxide

radical. For pure $\text{g-C}_3\text{N}_4$, when TEOA was added into the reaction, the degradation rate was greatly decrease indicating the holes play important role in the degradation reaction. When the reaction proceeded in the N_2 environment, the degradation rate is also slowed down indicating that the production of superoxide radical was depressed due to O_2 concentration is decreased in the solution. However, the hydroxyl radical has slightly effect on the degradation reaction. In the case of CC-1.0, we can find the holes and hydroxyl radical have similar behavior as pure $\text{g-C}_3\text{N}_4$. At the same time, N_2 also greatly depressed the degradation reaction indicating that superoxide effect is enhanced in the CC-1.0 system. It further illustrates that the superoxide radical is more easily produced in the CC-1.0 system. If it forms a heterojunction between Cu_3P and $\text{g-C}_3\text{N}_4$, the photogenerated hole will be transferred to Cu_3P . And then, the oxidative capability will be greatly decreased due to the VB of Cu_3P is about -0.14 eV. In other words, the hole cannot play the key role in the photocatalytic degradation reaction. On the other hand,

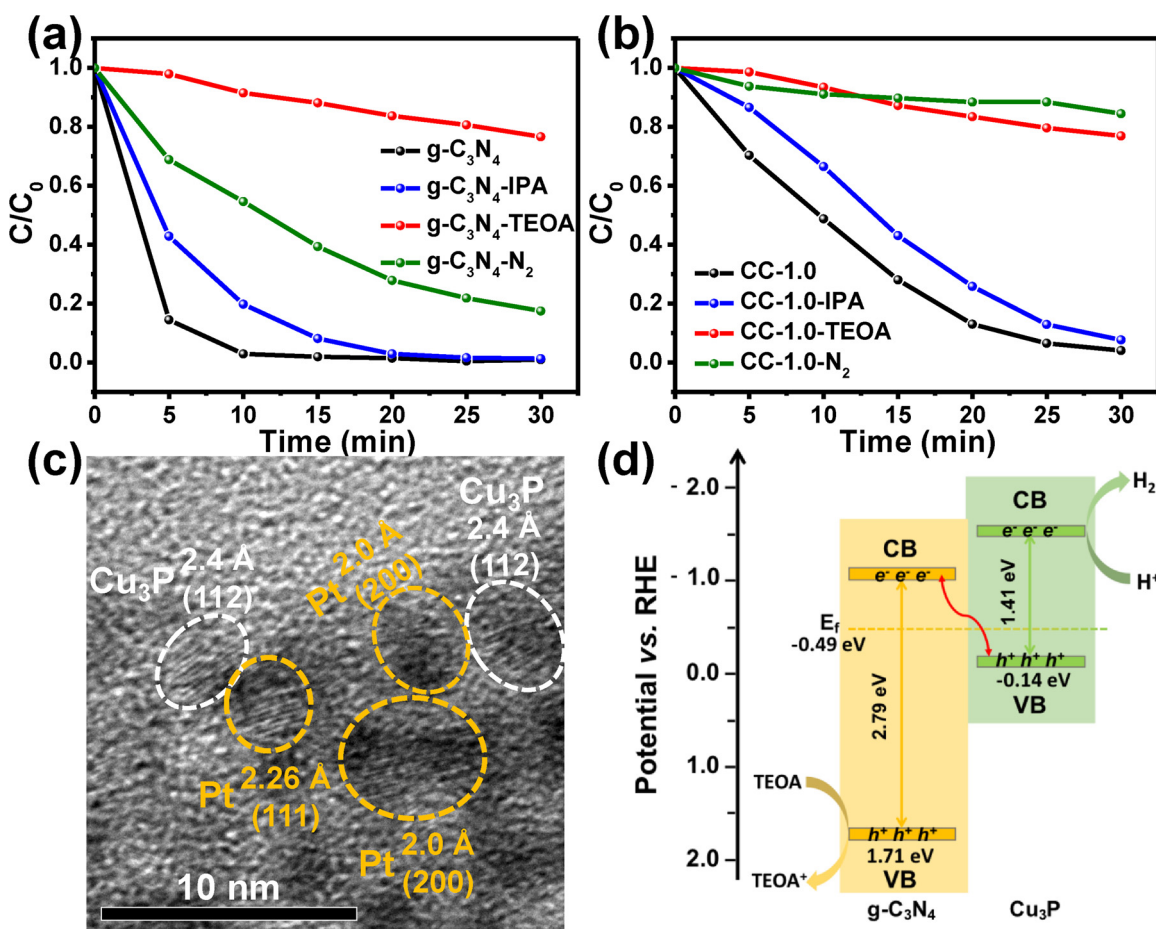


Fig. 6. The relative concentration change of rhodamine B (RhB) aqueous solution with visible light irradiation time in the presence of g-C₃N₄ (a) and CC-1.0 (b) with different scavengers (isopropanol alcohol (IPA), triethanol amine (TEOA)) or inhibitors (N₂). (c) HR TEM images of photodeposition of Pt nanoparticles on the CC-1.0. (d) the possible charge transfer mechanism for H₂ production for CC-1.0.

the photogenerated electron was transferred to the g-C₃N₄, then superoxide radical effect will similar to g-C₃N₄. Thus, we proposed that the photogenerated holes are kept on the g-C₃N₄, not transferred to the Cu₃P site. Furthermore, the photodeposition of noble metal Pt was carried out to disclose the site, where the photogenerated electron transfers. Fig. 6c shows the TEM images of Cu₃P/g-C₃N₄ loading Pt nanoparticles. Pt nanoparticles are found at the site, where is close to the Cu₃P nanoparticles, indicating that the photogenerated electrons are left on the Cu₃P, not transferred to the g-C₃N₄. Thus, we proposed that new charge transfer mechanism as shown in Fig. 6b for the Cu₃P/g-C₃N₄ catalyst. Under light irradiation, the p-type semiconductor nanoparticles produce more free holes due to cation vacancies [51]. The free hole is a favor to diffuse toward the space charge region. The photogenerated electron of g-C₃N₄ tends to transfer from g-C₃N₄ to the space charge region. Then they are recombined in the space charge region and left the electron on the Cu₃P for the hydrogen reduction reaction. The charge transfer route follows Z-scheme. That is the photogenerated electron from g-C₃N₄ recombines with the holes of Cu₃P, then the photogenerated electron of Cu₃P is left for H₂ production reaction. That provides a reasonable explanation for how the electron flow from g-C₃N₄ to the cocatalyst Cu₃P which has lower overpotential for H₂ reduction.

4. Conclusions

In summary, high surface area g-C₃N₄ was synthesized from thiourea with the aid of NH₄Cl as bubble maker. Cu₃P nanoparticles are loaded via CuCl(OH)₃ and phosphorization. Cu₃P/g-C₃N₄ photocatalyst

exhibits relatively high photocatalytic activity even with the trace amount of Cu₃P. To disclose the function of Cu₃P, various methods illustrate that Cu₃P has two functions in the catalyst system. One is promoting the charge separation, another is lowering the over-potential of HER. Thus, Cu₃P works as a cocatalyst for the composites. Furthermore, we investigate the charge transfer process for the Cu₃P/g-C₃N₄. The results indicate that the photogenerated electron was left on the Cu₃P site and hole was kept on g-C₃N₄. Based on this, we proposed the charge transfer route follows Z-scheme. That opens a door to explain the p-type semiconductor work as a cocatalyst in the photocatalyst system.

Acknowledgements

This work is supported by the Beijing Municipal High Level Innovative Team Building Program (IDHT20180504), Large-scale Instrument and Equipment Platform of Beijing University of Technology, the National Natural Science Foundation of China (21671011, 21872001, 21805004 and 51801006), Beijing High-level Talent program and Beijing Municipal Natural Science Foundation (KZ201710005002), the NSF of the Beijing Municipal Education Committee and Beijing Postdoctoral Research Foundation (2018-ZZ-021).

Appendix A. Supplementary data

Supplementary material related to this article can be found, in the online version, at doi:<https://doi.org/10.1016/j.apcatb.2018.09.010>.

References

[1] A. Fujishima, K. Honda, Electrochemical photolysis of water at a semiconductor electrode, *Nature* 238 (1972) 37–38.

[2] S.H.S. Chan, T.Y. Wu, J.C. Juan, C.Y. Teh, Recent developments of metal oxide semiconductors as photocatalysts in advanced oxidation processes (AOPs) for treatment of dye waste-water, *J. Chem. Technol. Biotechnol.* 86 (2011) 1130–1158.

[3] A.B. Djuricic, Y.H. Leung, A.M. Ching Ng, Strategies for improving the efficiency of semiconductor metal oxide photocatalysis, *Mater. Horizons* 1 (2014) 400–410.

[4] Y. Ma, X. Wang, Y. Jia, X. Chen, H. Han, C. Li, Titanium dioxide-based nanomaterials for photocatalytic fuel generations, *Chem. Rev.* 114 (2014) 9987–10043.

[5] G. Zhang, G. Liu, L. Wang, J.T.S. Irvine, Inorganic perovskite photocatalysts for solar energy utilization, *Chem. Soc. Rev.* 45 (2016) 5951–5984.

[6] X. Xu, C. Randorn, P. Efsthathiou, J.T.S. Irvine, A red metallic oxide photocatalyst, *Nat. Mater.* 11 (2012) 595.

[7] C. Martinez Suarez, S. Hernández, N. Russo, BiVO_4 as photocatalyst for solar fuels production through water splitting: a short review, *Appl. Catal. A Gen.* 504 (2015) 158–170.

[8] H. Li, J. Li, Z. Ai, F. Jia, L. Zhang, Oxygen vacancy-mediated photocatalysis of BiOCl : reactivity, selectivity, and perspectives, *Angew. Chem. Int. Ed.* 57 (2018) 122–138.

[9] H. Li, J. Shang, H. Zhu, Z. Yang, Z. Ai, L. Zhang, Oxygen vacancy structure associated photocatalytic water oxidation of BiOCl , *ACS Catal.* 6 (2016) 8276–8285.

[10] K. Zhang, L. Guo, Metal sulphide semiconductors for photocatalytic hydrogen production, *Catal. Sci. Technol.* 3 (2013) 1672–1690.

[11] A. Kudo, Y. Miseki, Heterogeneous photocatalyst materials for water splitting, *Chem. Soc. Rev.* 38 (2009) 253–278.

[12] J. Su, Y. Wei, L. Vayssières, Stability and performance of sulfide-, nitride-, and phosphide-based electrodes for photocatalytic solar water splitting, *J. Phys. Chem. Lett.* 8 (2017) 5228–5238.

[13] J. Yang, D. Wang, H. Han, C. Li, Roles of cocatalysts in photocatalysis and photoelectrocatalysis, *Acc. Chem. Res.* 46 (2013) 1900–1909.

[14] R.-B. Wei, Z.-L. Huang, G.-H. Gu, Z. Wang, L. Zeng, Y. Chen, Z.-Q. Liu, Dual-cocatalysts decorated rimous CdS spheres advancing highly-efficient visible-light photocatalytic hydrogen production, *Appl. Catal. B: Environ.* 231 (2018) 101–107.

[15] R.-B. Wei, P.-Y. Kuang, H. Cheng, Y.-B. Chen, J.-Y. Long, M.-Y. Zhang, Z.-Q. Liu, Plasmon-enhanced photoelectrochemical water splitting on gold nanoparticle decorated ZnO/CdS nanotube arrays, *ACS sustain. Chem. Eng.* 5 (2017) 4249–4257.

[16] P.Y. Kuang, P.X. Zheng, Z.Q. Liu, J.L. Lei, H. Wu, N. Li, T.Y. Ma, Embedding Au quantum dots in rimous cadmium sulfide nanospheres for enhanced photocatalytic hydrogen evolution, *Small* 12 (2016) 6735–6744.

[17] Y. Shi, B. Zhang, Recent advances in transition metal phosphide nanomaterials: synthesis and applications in hydrogen evolution reaction, *Chem. Soc. Rev.* 45 (2016) 1529–1541.

[18] S. Zhang, H. Yang, H. Gao, R. Cao, J. Huang, X. Xu, One-pot synthesis of CdS irregular nanospheres hybridized with oxygen-incorporated defect-rich MoS_2 ultra-thin nanosheets for efficient photocatalytic hydrogen evolution, *ACS Appl. Mater. Interfaces* 9 (2017) 23635–23646.

[19] Q. Zhang, Z. Li, S. Wang, R. Li, X. Zhang, Z. Liang, H. Han, S. Liao, C. Li, Effect of redox cocatalysts location on photocatalytic overall water splitting over cubic NaTaO_3 semiconductor crystals exposed with equivalent facets, *ACS Catal.* 6 (2016) 2182–2191.

[20] Z. Qin, Y. Chen, X. Wang, X. Guo, L. Guo, Intergrowth of cocatalysts with host photocatalysts for improved solar-to-Hydrogen conversion, *ACS Appl. Mater. Interfaces* 8 (2016) 1264–1272.

[21] J. Ran, J. Yu, M. Jaroniec, Ni(OH)_2 modified CdS nanorods for highly efficient visible-light-Driven photocatalytic H_2 generation, *Green Chem.* 13 (2011) 2708–2713.

[22] B. Qiu, Q. Zhu, M. Du, L. Fan, M. Xing, J. Zhang, Efficient Solar Light Harvesting $\text{CdS}/\text{Co}_9\text{S}_8$ Hollow Cubes for Z-Scheme Photocatalytic Water Splitting, *Angew. Chem. Int. Ed.* 56 (2017) 2684–2688.

[23] P. Chen, K. Xu, S. Tao, T. Zhou, Y. Tong, H. Ding, L. Zhang, W. Chu, C. Wu, Y. Xie, Phase-transformation engineering in cobalt diselenide realizing enhanced catalytic activity for hydrogen evolution in an alkaline medium, *Adv. Mater.* 28 (2016) 7527–7532.

[24] Y. Zhu, Y. Xu, Y. Hou, Z. Ding, X. Wang, Cobalt sulfide modified graphitic carbon nitride semiconductor for solar hydrogen production, *Int. J. Hydrogen Energy* 39 (2014) 11873–11879.

[25] S. Cao, Y. Chen, C.-J. Wang, P. He, W.-F. Fu, Highly efficient photocatalytic hydrogen evolution by nickel phosphide nanoparticles from aqueous solution, *Chem. Commun. (Camb.)* 50 (2014) 10427–10429.

[26] S. Cao, C.-J. Wang, W.-F. Fu, Y. Chen, Metal phosphides as Co-catalysts for photocatalytic and photoelectrocatalytic water splitting, *ChemSusChem* 10 (2017) 4306–4323.

[27] M. Liu, Y. Chen, J. Su, J. Shi, X. Wang, L. Guo, Photocatalytic hydrogen production using twinned nanocrystals and an unanchored Ni_{x} Co-catalyst, *Nat. Energy* 1 (2016) 16151.

[28] A. Indra, A. Acharjya, P.W. Menezes, C. Merschjann, D. Hollmann, M. Schwarze, M. Aktas, A. Friedrich, S. Lochbrunner, A. Thomas, M. Diess, Boosting visible-light-driven photocatalytic hydrogen evolution with an integrated nickel phosphide–carbon nitride system, *Angew. Chem. Int. Ed.* 56 (2017) 1653–1657.

[29] W. Wang, T. An, G. Li, D. Xia, H. Zhao, J.C. Yu, P.K. Wong, Earth-abundant $\text{Ni}_2\text{P}/\text{g-C}_3\text{N}_4$ lamellar nanohybrids for enhanced photocatalytic hydrogen evolution and bacterial inactivation under visible light irradiation, *Appl. Catal. B: Environ.* 217 (2017) 570–580.

[30] S. Cao, Y. Chen, C.-J. Wang, X.-J. Lv, W.-F. Fu, Spectacular photocatalytic hydrogen evolution using Metal-Phosphide/ CdS hybrid catalysts under sunlight irradiation, *Chem. Commun. (Camb.)* 51 (2015) 8708–8711.

[31] S.-S. Yi, J.-M. Yan, B.-R. Wulan, S.-J. Li, K.-H. Liu, Q. Jiang, Noble-metal-Free cobalt phosphide modified carbon nitride: an efficient photocatalyst for hydrogen generation, *Appl. Catal. B: Environ.* 200 (2017) 477–483.

[32] Z. Sun, H. Chen, Q. Huang, P. Du, Enhanced photocatalytic hydrogen production in water under visible light using noble metal-free ferrous phosphide as an active cocatalyst, *Catal. Sci. Technol.* 5 (2015) 4964–4967.

[33] H. Cheng, X.-J. Lv, S. Cao, Z.-Y. Zhao, Y. Chen, W.-F. Fu, Robustly Photogenerating H_2 in Water Using FeP/CdS Catalyst under Solar Irradiation, *Sci. Rep.* 6 (2016) 19846.

[34] A. Han, H. Chen, H. Zhang, Z. Sun, P. Du, Ternary metal phosphide nanosheets as a highly efficient electrocatalyst for water reduction to hydrogen over a wide pH range from 0 to 14, *J. Mater. Chem. A Mater. Energy Sustain.* 4 (2016) 10195–10202.

[35] L. Bi, X. Gao, L. Zhang, D. Wang, X. Zou, T. Xie, Enhanced photocatalytic hydrogen evolution of $\text{NiCoP}/\text{g-C}_3\text{N}_4$ with improved separation efficiency and charge transfer efficiency, *ChemSusChem* (2017).

[36] X. Yue, S. Yi, R. Wang, Z. Zhang, S. Qiu, A Novel and Highly Efficient Earth-Abundant Cu_3P with TiO_2 “p-n” Heterojunction Nanophotocatalyst for Hydrogen Evolution from Water, *Nanoscale* 8 (2016) 17516–17523.

[37] S. Hua, D. Qu, L. An, G. Xi, G. Chen, F. Li, Z. Zhou, Z. Sun, Highly dispersed few-layer MoS_2 nanosheets on S, N co-doped carbon for electrocatalytic H_2 production, *Chinese J. Catal.* 38 (2017) 1028–1037.

[38] K.S.W. Sing, D.H. Everett, R.A.W. Haul, L. Moscou, R.A. Pierotti, J. Rouquerol, T. Siemieniewska, Reporting physisorption data for Gas/Solid systems with special reference to the determination of surface area and porosity (Recommendations 1984), *Pure Appl. Chem.* 57 (1985) 603–619.

[39] Y. Wang, M.K. Bayazit, S.J.A. Moniz, Q. Ruan, C.C. Lau, N. Martsinovich, J. Tang, Linker-Controlled Polymeric Photocatalyst for highly Efficient Hydrogen Evolution from Water, *Energy Environ. Sci.* 10 (2017) 1643–1651.

[40] J. Li, B. Shen, Z. Hong, B. Lin, B. Gao, Y. Chen, A facile approach to synthesize novel oxygen-doped $\text{g-C}_3\text{N}_4$ with superior visible-light photoreactivity, *Chem. Commun. (Camb.)* 48 (2012) 12017–12019.

[41] X. Lu, K. Xu, P. Chen, K. Jia, S. Liu, C. Wu, Facile one step method realizing scalable production of $\text{g-C}_3\text{N}_4$ nanosheets and study of their photocatalytic H_2 evolution activity, *J. Mater. Chem. A Mater. Energy Sustain.* 2 (2014) 18924–18928.

[42] Z. Qin, M. Wang, R. Li, Y. Chen, Novel $\text{Cu}_3\text{P}/\text{g-C}_3\text{N}_4$ p-n heterojunction photocatalysts for solar hydrogen generation, *Sci. China Mater.* 61 (2018) 861–868.

[43] Z. Sun, B. Lv, J. Li, M. Xiao, X. Wang, P. Du, Core-shell amorphous cobalt Phosphide/Cadmium sulfide semiconductor nanorods for exceptional photocatalytic hydrogen production under visible light, *J. Mater. Chem. A Mater. Energy Sustain.* 4 (2016) 1598–1602.

[44] M. Liu, R. Zhang, L. Zhang, D. Liu, S. Hao, G. Du, A.M. Asiri, R. Kong, X. Sun, Energy-efficient electrolytic hydrogen generation using a Cu_3P nanoarray as a bi-functional catalyst for hydrazine oxidation and water reduction, *Inorgan. Chem. Front.* 4 (2017) 420–423.

[45] C.-C. Hou, Q.-Q. Chen, C.-J. Wang, F. Liang, Z. Lin, W.-F. Fu, Y. Chen, Self-Supported Cedarlike Semimetallic Cu_3P Nanoarrays as a 3D High-Performance Janus Electrode for Both Oxygen and Hydrogen Evolution under Basic Conditions, *ACS Appl. Mater. Interfaces* 8 (2016) 23037–23048.

[46] J. Chen, S. Shen, P. Guo, M. Wang, P. Wu, X. Wang, L. Guo, In-situ reduction synthesis of nano-sized Cu_2O particles modifying $\text{g-C}_3\text{N}_4$ for enhanced photocatalytic hydrogen production, *Appl. Catal. B: Environ.* 152–153 (2014) 335–341.

[47] Z. Sun, Q. Yue, J. Li, J. Xu, H. Zheng, P. Du, Copper phosphide modified cadmium sulfide nanorods as a novel p-n heterojunction for highly efficient visible-light-Driven hydrogen production in water, *J. Mater. Chem. A: Mater. Energy Sustain.* 3 (2015) 10243–10247.

[48] W. Cui, J. Li, Y. Sun, H. Wang, G. Jiang, S. Lee, F. Dong, Enhancing ROS generation and suppressing toxic intermediate production in photocatalytic NO oxidation on O/Ba Co-functionalized amorphous carbon nitride, *Appl. Catal. B: Environ.* 237 (2018) 938–946.

[49] J. Li, Q. Xing, Y. Zhou, H. Huang, F. Dong, The activation of reactants and intermediates promotes the selective photocatalytic NO conversion on electron-localized Sr-Intercalated $\text{g-C}_3\text{N}_4$, *Appl. Catal. B: Environ.* 232 (2018) 69–76.

[50] Y. Li, Y. Sun, W. Ho, Y. Zhang, H. Huang, Q. Cai, F. Dong, Highly enhanced visible-light photocatalytic NO_x purification and conversion pathway on self-structurally modified $\text{g-C}_3\text{N}_4$ nanosheets, *Sci. Bull. (Beijing)* 63 (2018) 609–620.

[51] A. Agrawal, S.H. Cho, O. Zandi, S. Ghosh, R.W. Johns, D.J. Milliron, Localized surface plasmon resonance in semiconductor nanocrystals, *Chem. Rev.* 118 (2018) 3121–3207.